Lowrank one-step wave extrapolation for reverse-time migration[a]

[a]Published in Geophysics, 81, no. 1, S39-S54, (2016)

Junzhe Sun[*1], *Sergey Fomel*[1] *and Lexing Ying*[2]

ABSTRACT

Reverse-time migration (RTM) relies on accurate wave extrapolation engines to image complex subsurface structures. To construct such operators with high efficiency and numerical stability, we propose an approach of one-step wave extrapolation using complex-valued lowrank decomposition to approximate the mixed-domain space-wavenumber wave extrapolation symbol. The lowrank one-step method involves a complex-valued phase function, which is more flexible than a real-valued phase function of two-step schemes, and thus is capable of modeling a wider variety of dispersion relations. Two novel designs of the phase function lead to desired properties in wave extrapolation. First, for wave propagation in inhomogeneous media, we include a velocity gradient term to implement a more accurate phase behavior, particularly when velocity variations are large. Second, we develop an absorbing boundary condition, which is propagation-direction-dependent and can be incorporated into the phase function as an anisotropic attenuation term. This term allows waves to travel parallel to the boundary without absorption, thus reducing artificial reflections at wide-incident angles. Using numerical experiments, we demonstrate the stability improvement of a one-step scheme in comparison with two-step schemes. We observe the lowrank one-step operator to be remarkably stable and capable of propagating waves using large time step sizes, even beyond the Nyquist limit. The stability property can help minimize the computational cost of seismic modeling or reverse-time migration. We also demonstrate that lowrank one-step wave extrapolation handles anisotropic wave propagation accurately and efficiently. When applied to RTM in anisotropic media, the proposed method generates high quality images.

INTRODUCTION

The task of wave extrapolation is propagation of waves in depth or time, which finds applications in seismic modeling and migration. Conventionally, it is implemented by finite differences (FD). FD methods have a low computational cost but suffer from dispersion artifacts and instabilities (Kosloff and Baysal, 1982). Instead, numerical differentiation of space coordinates in wave equations can be implemented by employing the Fourier transform, which are known as pseudo-spectral methods (Fornberg, 1998). Pseudo-spectral methods

[1]Parts of this paper were presented at 2013 SEG meeting

have higher accuracy and can suppress numerical dispersion (Reshef et al., 1988; Virieux et al., 2011). On the other hand, they are limited to small time steps and may be subject to dispersion because of finite-difference approximations used for the time derivatives. Recently, alternative strategies have been proposed to propagate waves by mixed-domain space-wavenumber operators (Soubaras and Zhang, 2008; Wards et al., 2008; Etgen and Brandsberg-Dahl, 2009; Liu et al., 2009; Zhang and Zhang, 2009; Du et al., 2010; Pestana and Stoffa, 2010; Chu and Stoffa, 2011; Fomel et al., 2013; Wu and Alkhalifah, 2014). Fowler et al. (2010b) and Du et al. (2014) referred to these methods as recursive integral time extrapolation (RITE) methods.

RITE methods are designed to make time extrapolation both stable and dispersion free in heterogeneous media for large time steps, even beyond the Nyquist limit (Du et al., 2014), and therefore are particularly suitable for reverse-time migration (RTM), a depth-migration method in which waves are extrapolated in time (Baysal et al., 1983; McMechan, 1983; Whitmore, 1983; Farmer et al., 2006; Fletcher et al., 2009; Fowler et al., 2010a). RTM performs imaging by solving the two-way wave equation in the most straightforward manner compared with other methods, and therefore is capable of handling complicated wave forms, such as prismatic waves, and generating images free of artifacts that are caused by approximations of the physics of wave propagation in other methods (Etgen et al., 2009; Leveille et al., 2011). The efficiency of RTM thus relies on the wave propagation engine.

Among the different RITE approaches, the lowrank wave extrapolation (Fomel et al., 2010, 2013) distinguishes itself by its high efficiency and flexible control over approximation accuracy. Lowrank approximation has been implemented under different frameworks, including lowrank finite differences and lowrank Fourier finite differences (Song et al., 2013; Fang et al., 2014). A lowrank algorithm decomposes the original mixed-domain wave propagation matrix into a small set of representative spatial locations and a small set of representative wavenumbers. Similar to other spectral methods, the cost of computation per time step with the lowrank method is $O(N\,N_x\,\log N_x)$, where N_x is the total size of the computational grid and N is a small number (the rank of the approximation) controlling the trade-off between accuracy and efficiency.

Fomel et al. (2013) implemented lowrank wave extrapolation using a two-step time marching scheme, which involves a real-valued wave propagation operator. The application of a two-step scheme is constrained by its requirement of a real-valued phase function. In this paper, we propose adopting a one-step scheme, which propagates a complex-valued wavefield using a complex phase function. Following Zhang and Zhang (2009), we show that separation of forward- and backward-propagating waves can be achieved by constructing a complex wavefield, with its imaginary part being the Hilbert transform of the real part. The complex wavefield corresponds to the analytical signal (Taner et al., 1979). In practice, the proposed one-step scheme demonstrates significantly improved stability. Its ability to extrapolate waves using large time steps should help reduce the cost of computationally intensive tasks, such as RTM and time-domain full waveform inversion (FWI). A complex-valued phase function is capable of incorporating modified forms of dispersion relations. In particular, we show that, by including a velocity gradient term into the approximation of phase function, the accuracy of wave extrapolation can be improved in media with large velocity variations. Additionally, we propose a propagation-direction-dependent absorbing boundary condition that can be incorporated into the complex-valued phase function. This condition behaves like an anisotropic attenuation term, which attenuates waves preferen-

cially in the direction perpendicular to the absorbing boundary, thus reducing artificial reflections at wide incident angles. Such modifications of the phase function take advantage of the complex-valued symbol in the one-step scheme. The proposed method is easily extended to anisotropic wave propagation, such as tilted transversely isotropic (TTI) or orthorhombic media, without producing unwanted residual shear-wave energy (Du et al., 2014). We use numerical examples with synthetic models to test the accuracy, efficiency and stability of the proposed lowrank one-step wave extrapolation method. Finally, we apply lowrank one-step RTM to the BP 2007 TTI synthetic data set to test its ability of producing high-quality seismic images.

THEORY

Let $p(\mathbf{x},t)$ be the seismic wavefield at location $\mathbf{x}$ and time t. The acoustic constant-density wave equation can be written as

$$\left(\frac{\partial^2}{\partial t^2} - V^2(\mathbf{x})\nabla^2\right) p(\mathbf{x},t) = 0 \ , \tag{1}$$

where $V(\mathbf{x})$ is velocity and ∇^2 denotes the Laplacian operator.

Analytical solutions in constant velocity

When V is constant, after Fourier transform in space, the wave equation takes the form

$$\left(\frac{\partial^2}{\partial t^2} + V^2|\mathbf{k}|^2\right) P(\mathbf{k},t) = 0 \ , \tag{2}$$

where $\mathbf{k}$ is the spatial wavenumber and $P(\mathbf{k},t)$ is the spatial Fourier transform of $p(\mathbf{x},t)$:

$$P(\mathbf{k},t) = \frac{1}{(2\pi)^3}\int p(\mathbf{x},t)e^{-i\mathbf{k}\cdot\mathbf{x}}d\mathbf{x} \ . \tag{3}$$

The analytical solution to equation 2 can be expressed as

$$P = A_1 e^{i|\mathbf{k}|Vt} + A_2 e^{-i|\mathbf{k}|Vt} = P_1 + P_2 \ , \tag{4}$$

where P_1 represents the forward-propagating wavefield, i.e., positive frequencies, and P_2 represents the backward-propagating wavefield, i.e., negative frequencies. The time derivative of P has the following form:

$$\frac{\partial P}{\partial t} = i|\mathbf{k}|V(P_1 - P_2) \ . \tag{5}$$

Zhang and Zhang (2009) used the Hilbert transform to define an additional function:

$$Q(\mathbf{k},t) = \frac{1}{\psi}\frac{\partial P(\mathbf{k},t)}{\partial t} \ , \tag{6}$$

where $Q(\mathbf{k},t)$ is the Hilbert transform of $P(\mathbf{k},t)$, and $\psi = V|\mathbf{k}|$. Combining equations 4, 5 and 6, P_1 and P_2 can be expressed as

$$P_1 = \frac{1}{2}\left(P - iQ\right) \ , \tag{7}$$

$$P_2 = \frac{1}{2}\left(P + iQ\right) \ . \tag{8}$$

Equation 2 can be split into a pair of first-order equations and expressed in the following matrix form:

$$\frac{\partial}{\partial t}\begin{bmatrix} P \\ P_t \end{bmatrix} = \begin{bmatrix} 0 & 1 \\ -\psi^2 & 0 \end{bmatrix} \begin{bmatrix} P \\ P_t \end{bmatrix} . \tag{9}$$

With the help of the Hilbert transform and equations 7 and 8, a more symmetric expression can be achieved:

$$\frac{\partial}{\partial t}\begin{bmatrix} P \\ iQ \end{bmatrix} = \begin{bmatrix} 0 & -i\psi \\ -i\psi & 0 \end{bmatrix} \begin{bmatrix} P \\ iQ \end{bmatrix} . \tag{10}$$

We can further decompose the first matrix on the right-hand side as follows:

$$\begin{bmatrix} 0 & -i\psi \\ -i\psi & 0 \end{bmatrix} = \begin{bmatrix} 1 & 1 \\ -1 & 1 \end{bmatrix} \begin{bmatrix} i\psi & 0 \\ 0 & -i\psi \end{bmatrix} \begin{bmatrix} 1/2 & -1/2 \\ 1/2 & 1/2 \end{bmatrix} . \tag{11}$$

Substituting equation 11 into equation 10, and using equations 7 and 8, we arrive at:

$$\frac{\partial}{\partial t}\begin{bmatrix} P \\ iQ \end{bmatrix} = \begin{bmatrix} 1 & 1 \\ -1 & 1 \end{bmatrix} \begin{bmatrix} i\psi & 0 \\ 0 & -i\psi \end{bmatrix} \begin{bmatrix} P_1 \\ P_2 \end{bmatrix} . \tag{12}$$

In RTM, only one branch of the total wavefield is needed at one time. The two parts of wave propagation decouple according to

$$\frac{\partial}{\partial t}\begin{bmatrix} P_1 \\ P_2 \end{bmatrix} = \begin{bmatrix} i\psi & 0 \\ 0 & -i\psi \end{bmatrix} \begin{bmatrix} P_1 \\ P_2 \end{bmatrix} . \tag{13}$$

Modeling seismic wave propagation requires the source function. Letting the source function be $f(\mathbf{x}, t)$, wave equation 2 can be rewritten in the following form:

$$\left(\frac{\partial^2}{\partial t^2} + \psi^2\right) P(\mathbf{k}, t) = \hat{f}(\mathbf{k}, t) . \tag{14}$$

Correspondingly, equation 13 becomes:

$$\begin{aligned} \frac{\partial}{\partial t}\begin{bmatrix} P_1 \\ P_2 \end{bmatrix} &= \begin{bmatrix} 1/2 & -1/2 \\ 1/2 & 1/2 \end{bmatrix} \left\{ \begin{bmatrix} 0 & -i\psi \\ -i\psi & 0 \end{bmatrix} \begin{bmatrix} P \\ iQ \end{bmatrix} + \begin{bmatrix} 0 \\ \frac{i}{\psi}\hat{f} \end{bmatrix} \right\} \\ &= \begin{bmatrix} i\psi & 0 \\ 0 & -i\psi \end{bmatrix} \begin{bmatrix} P_1 \\ P_2 \end{bmatrix} + \begin{bmatrix} -\frac{i}{2\psi}\hat{f} \\ \frac{i}{2\psi}\hat{f} \end{bmatrix} . \end{aligned} \tag{15}$$

The application of operator $-i/2\psi$ can be implemented in either time domain or Fourier domain; it can also be directly incorporated into the definition of source functions. For example, operator $1/\psi$ can be regarded as $(i\omega/|\omega|) \cdot (1/i\omega)$, which in the time domain corresponds to cascading the Hilbert-transform with the first-order integration.

In constant velocity, the forward-propagating wavefield away from the source at the next time step $t + \Delta t$ can be expressed as:

$$p_1(\mathbf{x}, t + \Delta t) = \int P_1(\mathbf{k}, t)\, e^{i\,[\mathbf{k}\cdot\mathbf{x} + V\,|\mathbf{k}|\,\Delta t]}\, d\mathbf{k} . \tag{16}$$

Variable velocity and anisotropy

For inhomogeneous and anisotropic media, we can use the general form of equation 16 to introduce a general phase function, which depends on both $\mathbf{k}$ and $\mathbf{x}$, and rewrite equation 16 as the following mixed-domain operator (Wards et al., 2008; Fomel et al., 2013):

$$p_1(\mathbf{x}, t+\Delta t) = \int P_1(\mathbf{k}, t)\, e^{i\,\phi(\mathbf{x},\mathbf{k},\Delta t)}\, d\mathbf{k}\ . \tag{17}$$

Equation 17 is kinematically correct if the phase function $\phi(\mathbf{x}, \mathbf{k}, t)$ satisfies the anisotropic eikonal equation:

$$\frac{\partial \phi}{\partial t} = \pm V(\mathbf{x}, \mathbf{k})\ |\nabla \phi|\ , \tag{18}$$

where $V(\mathbf{x}, \mathbf{k})$ is the phase velocity. When velocity is constant and isotropic, the phase function reduces to

$$\phi(\mathbf{x}, \mathbf{k}, t) = \mathbf{k}\cdot\mathbf{x} \pm V|\mathbf{k}|\ , \tag{19}$$

and corresponds to equation 16. In the more general case, assuming small time steps, ϕ can be expanded into the Taylor series in t (Fomel et al., 2013):

$$\phi(\mathbf{x}, \mathbf{k}, t) \approx \mathbf{k}\cdot\mathbf{x} + \phi_1(\mathbf{x}, \mathbf{k})\, t + \phi_2(\mathbf{x}, \mathbf{k})\, \frac{t^2}{2} + \cdots\ , \tag{20}$$

where

$$\phi_1(\mathbf{x}, \mathbf{k}) = V(\mathbf{x}, \mathbf{k})\, |\mathbf{k}|\ , \tag{21}$$

$$\phi_2(\mathbf{x}, \mathbf{k}) = V(\mathbf{x}, \mathbf{k})\, \nabla V \cdot \mathbf{k}\ . \tag{22}$$

Equation 17 corresponds to the one-step method (Zhang and Zhang, 2009; Fowler et al., 2010b). Fomel et al. (2013) adopted instead a two-step implementation, which uses only the ϕ_1 term in equation 20 to cancel out the imaginary part of the wave extrapolation operator (Etgen and Brandsberg-Dahl, 2009):

$$p(\mathbf{x}, t+\Delta t) + p(\mathbf{x}, t-\Delta t) \approx 2 \int P(\mathbf{k}, t)\, e^{i\,\mathbf{k}\cdot\mathbf{x}} \cos\left[V(\mathbf{x}, \mathbf{k})\, |\mathbf{k}|\, \Delta t\right]\, d\mathbf{k}\ . \tag{23}$$

It is important to realize that the cancellation of the imaginary part relies on the fact that the phase function only contains odd-order terms of t, with the exception of the zeroth-order term which corresponds to the inverse Fourier transform. Any modification to the phase function that violates this requirement cannot be easily handled by the two-step method.

As detailed in the appendix, the unconditional numerical stability of the one-step scheme (equation 17) can be proven theoretically in the continuous cace. In practice, we have observed that the lowrank approximation preserves the stability property, as will be demonstrated in the next section with numerical examples.

Higher-order terms from the phase function

In this paper, we adopt the one-step scheme due to its superior stability and ability to handle complex-valued phase functions. Because the two-step scheme depends on a real-valued phase function, it cannot include higher-order terms from the expansion (equation 20)

and implement more accurate phase functions. By switching to a one-step scheme, we can easily incorporate the second-order term (ϕ_2) in equation 20 to achieve a more accurate wave extrapolation operator. As defined in equation 22, ϕ_2 involves the gradient of the velocity model, and can become significant when either the time step size is large or the velocity model changes rapidly. Substituting the first three terms from the Taylor series (equation 20) into equation 17, the second-order operator takes the form

$$p_1(\mathbf{x}, t+\Delta t) \approx \int P_1(\mathbf{k}, t)\, e^{i\left[\mathbf{k}\cdot\mathbf{x} + V(\mathbf{x},\mathbf{k})\,|\mathbf{k}|\,\Delta t + V(\mathbf{x},\mathbf{k})\,\nabla V\cdot\mathbf{k}\Delta t^2/2\right]}\, d\mathbf{k}\ . \tag{24}$$

This modification helps increase the accuracy of wave extrapolation, especially when Δt or ∇V are large. Note that the introduction of the velocity gradient term does require the velocity model to be smoothly varying, which conforms to the usual requirement of RTM. The term $\nabla V \cdot \mathbf{k}$ also leads to a certain degree of anisotropy in the phase function, which in practice may increase the numerical rank of lowrank approximation.

Direction-dependent absorbing boundary conditions

We propose another innovation using the one-step scheme by incorporating propagation-direction-dependent absorbing boundary conditions into the extrapolation operator. In absorbing boundary layers, we propose to modify the operator

$$W(\mathbf{x}, \mathbf{k}) = e^{i\,[\phi(\mathbf{x},\mathbf{k},\Delta t) - \mathbf{k}\cdot\mathbf{x}]} \tag{25}$$

into the following form:

$$W(\mathbf{x}, \mathbf{k})_{abc} = e^{i\,[\phi(\mathbf{x},\mathbf{k},\Delta t) - \mathbf{k}\cdot\mathbf{x}] - [\frac{\alpha(\mathbf{x}-\mathbf{x_t})\cdot\mathbf{k}}{|\mathbf{k}|}]^2}\ , \tag{26}$$

where α is the decay parameter and $\mathbf{x_t}$ is the location of the nearest absorbing boundary. The added term $e^{-[\frac{\alpha(\mathbf{x}-\mathbf{x_t})\cdot\mathbf{k}}{|\mathbf{k}|}]^2}$ causes exponential decay of the wavefield between the absorbing boundary and the computational boundary (domain truncation), which also depends on the wave traveling direction. When the wave travels normal to the boundary, it will have the maximum absorbing effect because $\mathbf{x} - \mathbf{x_t}$ is in the direction of $\mathbf{k}$; on the other hand, there will be no damping when the wave is traveling parallel to the boundary, as the angle between $\mathbf{x} - \mathbf{x_t}$ and $\mathbf{k}$ would be zero. Allowing waves to propagate within the absorbing zone can mitigate artificial reflections from the absorbing boundary, especially at grazing incident angles. The decay term should be applied on both the real wavefield and its first-order time derivative (the imaginary part of the analytical wavefield). This is analogous to the tapering technique described by Cerjan et al. (1985). The absorbing term in the phase function can be physically interpreted as an anisotropic attenuation effect.

The proposed direction-dependent absorbing boundary conditions could also be incorporated into two-step based wave extrapolation methods (Fomel et al., 2013; Song et al., 2013; Fang et al., 2014) using lowrank approximation, by separately applying the damping operator on both the wavefield and its time derivative. However, since two-step schemes do not allow a direct incorporation of the absorbing boundary condition into the wave propagation matrix, additional Fourier transforms will be required. The one-step implementation is more computationally efficient and straightforward.

Lowrank approximation

To implement wave propagation numerically, we employ the lowrank approximation method of Fomel et al. (2013) to decompose the wave extrapolation matrix 26 into the following separated representation:

$$W(\mathbf{x},\mathbf{k}) \approx \sum_{m=1}^{M}\sum_{n=1}^{N} W(\mathbf{x},\mathbf{k}_m)a_{mn}W(\mathbf{x}_n,\mathbf{k}). \tag{27}$$

The difference is that now the lowrank decomposition is implemented for complex matrices or linear operators instead of real ones. The computation of $p(\mathbf{x},t+\Delta t)$ then becomes:

$$p(\mathbf{x},t+\Delta t) \approx \sum_{m=1}^{M} W(\mathbf{x},\mathbf{k}_m)\left(\sum_{n=1}^{N} a_{mn}\left(\int e^{i\mathbf{x}\mathbf{k}}W(\mathbf{x}_n,\mathbf{k})P(\mathbf{k},t)d\mathbf{k}\right)\right) . \tag{28}$$

The computational cost of representation 28 is effectively equivalent to applying N inverse fast Fourier transforms per time step. In practice, N is a small number, typically less than 5 for isotropic media. N may grow with increasing model complexity, such as the introduction of anisotropy. Compared with a naive straightforward implementation of equation 17, the number of floating point operations per time step is reduced from $O(N_x^2)$ to $O(N\,N_x\,\log N_x)$, where N_x is the total size of the spatial grid.

RTM imaging conditions

Since the one-step wave extrapolation kernel operates in the complex domain, it requires a definition of data and reflectivity with complex values. The analytical data follows the definition of the complex wavefield in equations 7 and 8. It implies that the input data need to be Hilbert-transformed along the time axis and supplied as the imaginary part before the migration process, creating an analytical signal (Taner et al., 1979). We adopt the following complex-valued cross-correlation imaging condition (Claerbout, 1985):

$$I_c(\mathbf{x}) = \sum_s \sum_t \bar{S}_s(\mathbf{x},t)\, R_s(\mathbf{x},t)\ , \tag{29}$$

where the lower case s denotes shots and t denotes time samples. The real part of the complex image $I_c(\mathbf{x})$ is extracted and used as the final image.

Extended imaging conditions (Sava and Vasconcelos, 2011), including space-shift (Rickett and Sava, 2002; Sava and Fomel, 2003) and time-shift (Sava and Fomel, 2006) imaging conditions, can provide additional information for migration velocity analysis. The complex-valued space-shift and time-shift imaging condition for lowrank one-step RTM takes the form

$$I_e(\mathbf{x},\lambda,\tau) = \sum_s \sum_t \bar{S}_s(\mathbf{x}-\lambda,t-\tau)\, R_s(\mathbf{x}+\lambda,t+\tau) \tag{30}$$

and can be easily implemented in the time-space domain.

EXAMPLES

In this section, we use several numerical examples to demonstrate the properties of lowrank one-step wave extrapolation.

Complex-valued Lowrank Approximation

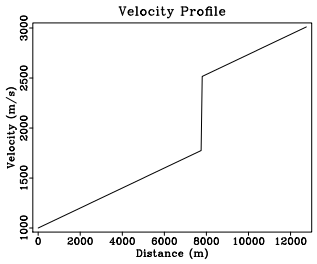

Figure 1: One-dimensional velocity profile with a sharp interface. fio1d/ vel1d

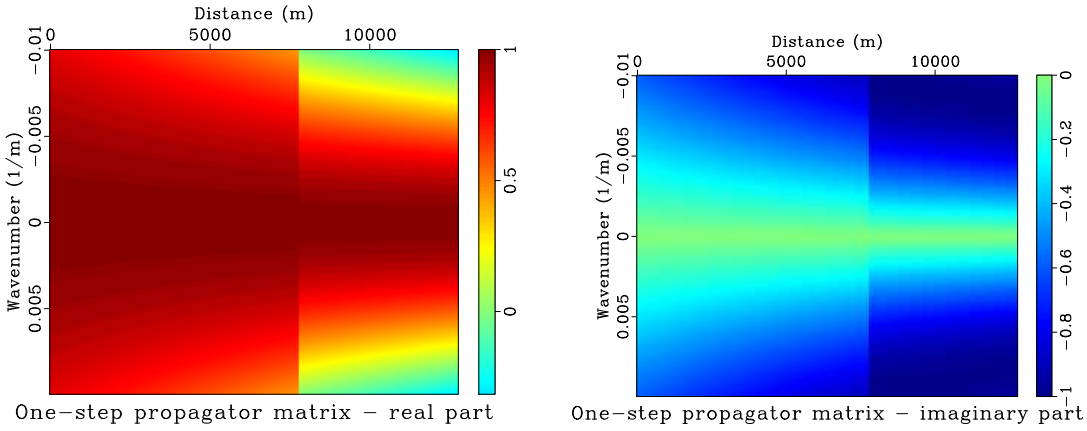

(a) (b)

Figure 2: (a) The real part of the wave extrapolation matrix; (b) the imaginary part of wave extrapolation matrix. fio1d/ propr,propi

We first test the accuracy of lowrank approximation applied to wave extrapolation matrix in a 1D inhomogeneous medium. Using a simple velocity profile with a sharp velocity contrast (Figure 1), and a time step size of 0.01 s, the real and imaginary part of the wave extrapolation matrix defined by Equation 25 with only the ϕ_1 term are plotted in Figures 2a and 2b, respectively. An accuracy threshold of $\epsilon = 10^{-4}$ leads to an approximation rank $N = 4$. The approximation error is plotted in Figures 3a and 3b and shows the maximum error corresponding to the prescribed accuracy requirement. To see that the accuracy threshold is strick enough to guarantee kinematic accuracy, we first use an exact matrix multiplication to calculate the exact wavefield from an initial condition (Figure 4a). Next, we use lowrank wave extrapolation to compute the wavefield and calculate their difference (Figure 4b). Negligible error can be observed from the difference section, indicating the high accuracy of lowrank wave extrapolation.

Two-layer Model

We use a simple two-layer velocity model similar to the one used by Du et al. (2014) to demonstrate the stability of one-step wave extrapolation using lowrank approximation. Figure 5 shows the comparison among the stability of lowrank one-step, lowrank two-step and fourth-order FD methods. The velocity model has a sharp contrast at the depth of 3795 m; the upper layer has a velocity of 1500 m/s, and the lower layer has a velocity of

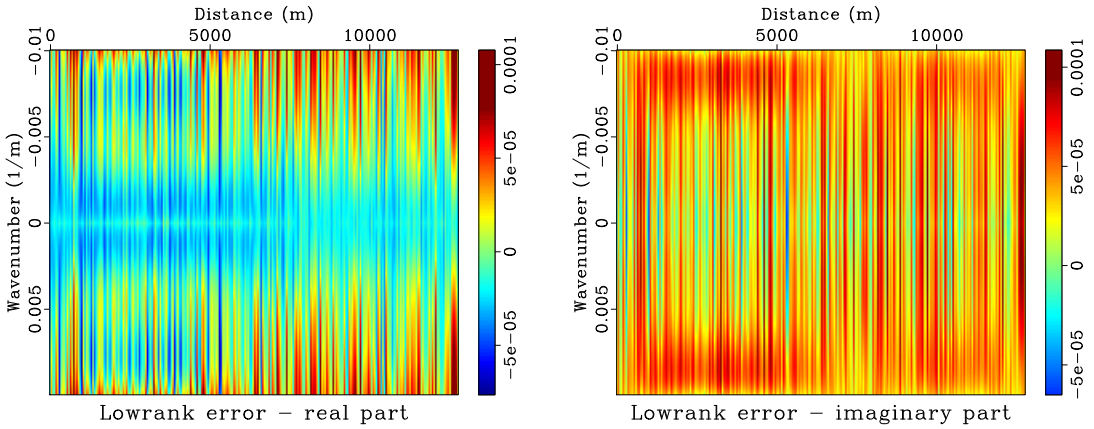

(a) (b)

Figure 3: (a) The real part of the approximation error; (b) the imaginary part of the approximation error. fio1d/ proderr1r,proderr1i

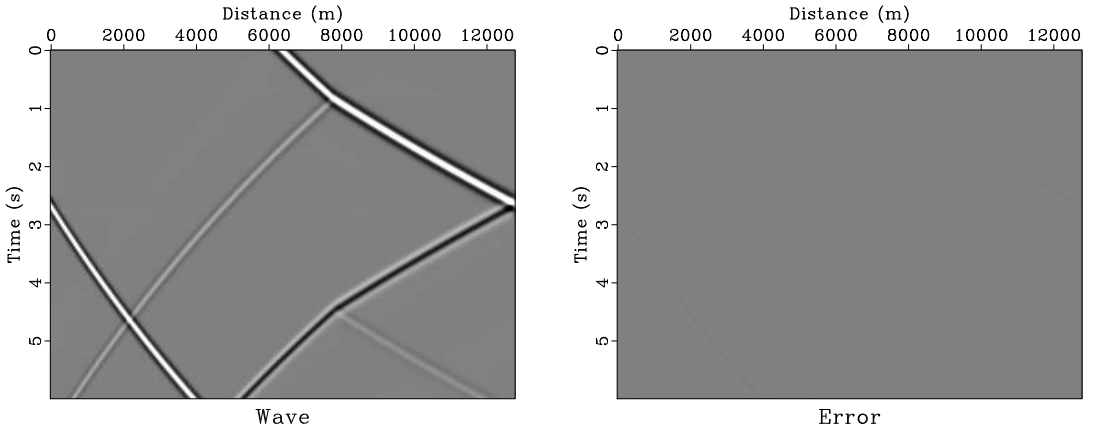

(a) (b)

Figure 4: (a) 1D wave propagation from an initial condition - exact solution; (b) error of lowrank wave extrapolation. fio1d/ wave2,error

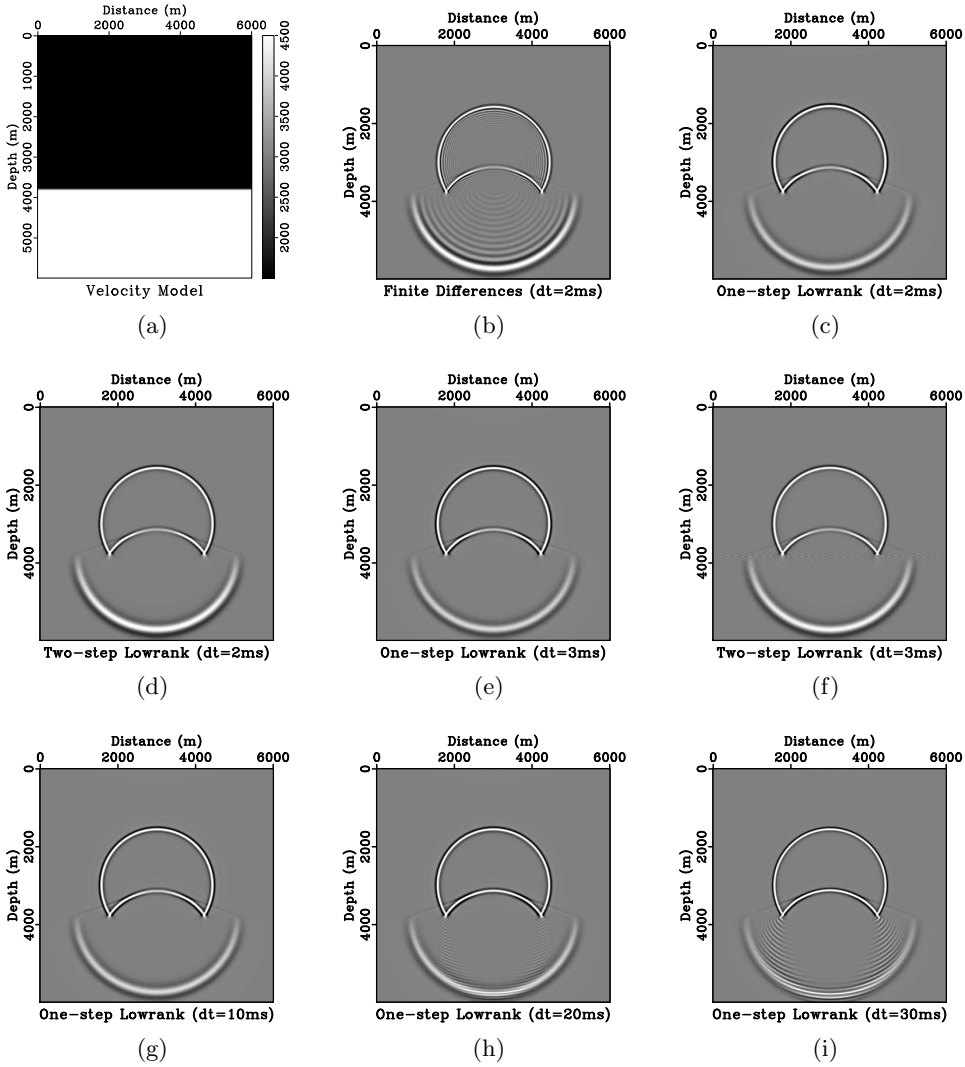

Figure 5: Stability comparison between different schemes. Wavefield snapshots are taken at $t = 1.1\ s$. (a) Two-layer velocity model. Velocity is 1500 m/s in the top layer and 4500 m/s in the bottom layer. (b) Wavefield modeled by FD with $\Delta t = 2\ ms$. (c) Wavefield modeled by the one-step scheme with $\Delta t = 2\ ms$. (d) Wavefield modeled by the two-step scheme with $\Delta t = 2\ ms$. (e) Wavefield modeled by the one-step scheme with $\Delta t = 3\ ms$. (f) Wavefield modeled by the two-step scheme with $\Delta t = 3\ ms$. (g) Wavefield modeled by the one-step scheme with $\Delta t = 10\ ms$. (h) Wavefield modeled by the one-step scheme with $\Delta t = 20\ ms$. (i) Wavefield modeled by the one-step scheme with $\Delta t = 30\ ms$. fowler/ twolayer,fwavefd,wave1-2,wave2-2,wave1-3,wave2-3,wave1-10,wave1-20,wave1-30

4500 m/s (Figure 5a). The model is discretized on a 400×400 grid with a spacing of 15 m along both horizontal and vertical directions. An explosive source, with a Ricker wavelet using a peak frequency of 16 Hz (maximum frequency approximately 50 Hz) is injected in the center of the model. When a time step of 2 ms is used, the classic fourth-order FD method suffers from visible dispersion artifacts (Figure 5b), whereas both the one-step and two-step schemes produce waves free of artifacts (Figure 5c and 5d). When a time step of 3 ms is used, the one-step scheme is stable (Figure 5e) whereas the two-step scheme starts to develop artifacts near the velocity contrast (Figure 5f). The FD method is no longer stable and therefore is not plotted. At 10 ms, which corresponds to the Nyquist sampling rate, the one-step scheme remains stable (Figure 5g), but the two-step scheme becomes unstable and thus is not plotted. Using 20 ms, the one-step scheme is still stable, but starts to develop ringing artifacts similar to those observed by Du et al. (2014) (Figure 5h). Using the time step size of 30 ms, the ringing effects aggravate, however the operator remains stable (Figure 5i).

Improved phase accuracy

To test if a more accurate wavefield can be obtained by using one-step extrapolation with equation 24, we first use a synthetic model with a smooth velocity distribution and large velocity variations (Figure 6a). We propagate a wavefield with the Ricker-wavelet source, using a time step of 3.5 ms. The model is discretized on a 512×512 grid with a spacing of 5 m along both horizontal and vertical directions. The source is injected in the center of the model. Figure 6b shows the reference wavefield propagated using only the ϕ_1 term from equation 20, but with an exceedingly small time step (0.175 ms), so that the ϕ_2 term is negligible and the wavefield can be treated as accurate. Figure 6c shows the difference between the reference wavefield and the wavefield propagated by equation 24 after normalization. Figure 6d shows the difference between the reference wavefield and the wavefield propagated without including the ϕ_2 term in the phase function, also after normalization. After including the velocity-gradient term, the error decreases significantly, and is caused mainly by small amplitude differences. On the other hand, the difference calculated without using the velocity-gradient term is due mostly to the shift in phase. This observation is further supported by Figure 7, which shows a comparison between traces extracted from the 2D wavefield snapshots at $X = 2000$ m. The trace calculated using the velocity-gradient term aligns with the reference trace, whereas the trace calculated without including the velocity-gradient term has a noticeable shift in space relative to the reference trace. The shift increases with the degree of velocity variation.

Next, we perform a similar experiment using a more complicated Marmousi velocity model (Figure 8a). The model is smoothed and discretized on a 376×576 grid with a spacing of 25 m. The reference wavefield is propagated using a time step size of 1.5 ms (Figure 8b). Figures 8c and 8d demonstrates the difference between the reference wavefield and the wavefields calculated using phase functions with and without the velocity gradient term. Figure 9 overlays the trace from the reference wavefield extracted at $Z = 8800$ m with corresponding traces from the wavefields propagated using a larger time step size. The comparison shows that, even with moderate velocity variations but a relatively large time step size, the velocity gradient term can have a noticeable contribution to the phase accuracy.

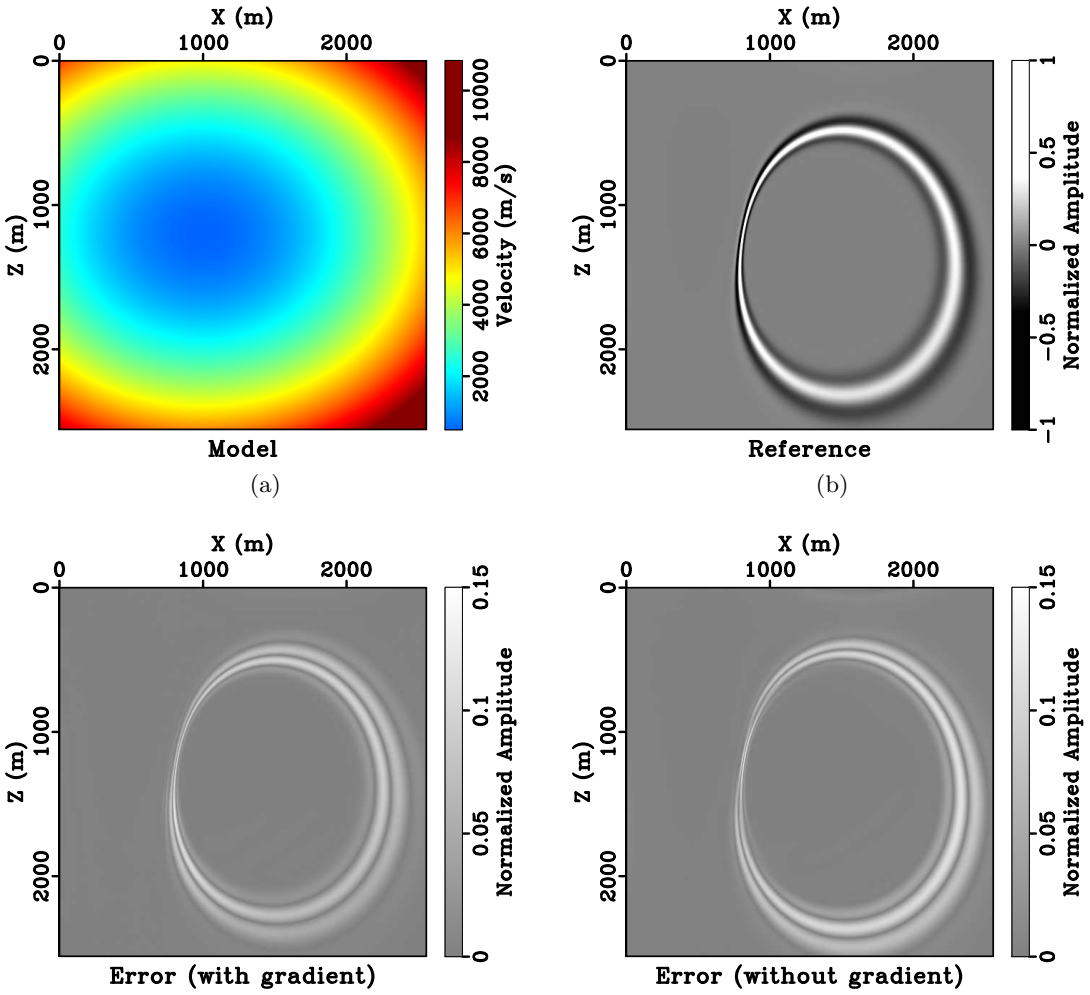

Figure 6: Wave propagation in a medium with large velocity variations. (a) Velocity model. (b) Reference wavefield propagated using $\Delta t = 0.175\ ms$. (c) Difference between reference and wavefield propagated with the velocity-gradient term using $\Delta t = 3.5\ ms$. (d) Difference between reference and wavefield propagated without the velocity-gradient term using $\Delta t = 3.5\ ms$. grad/ vel,wave2snap,diff,diff1

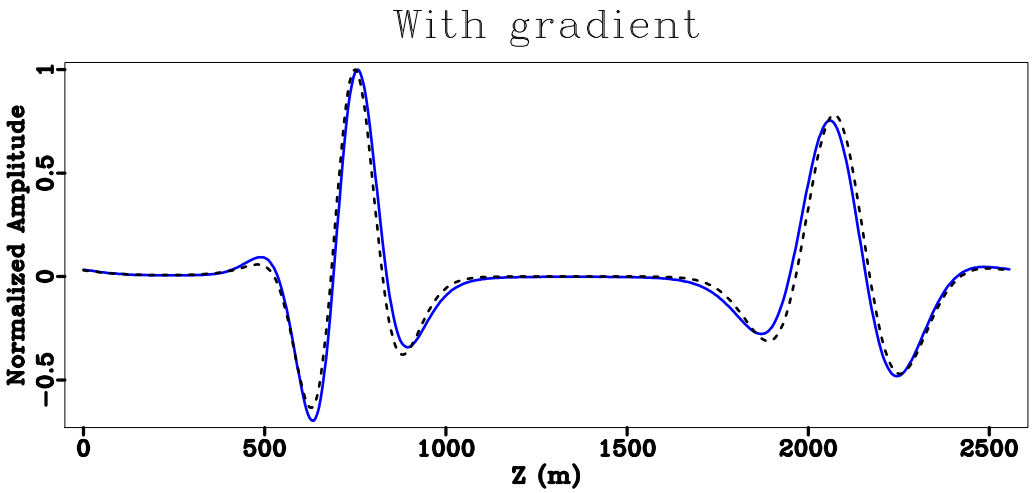

(a)

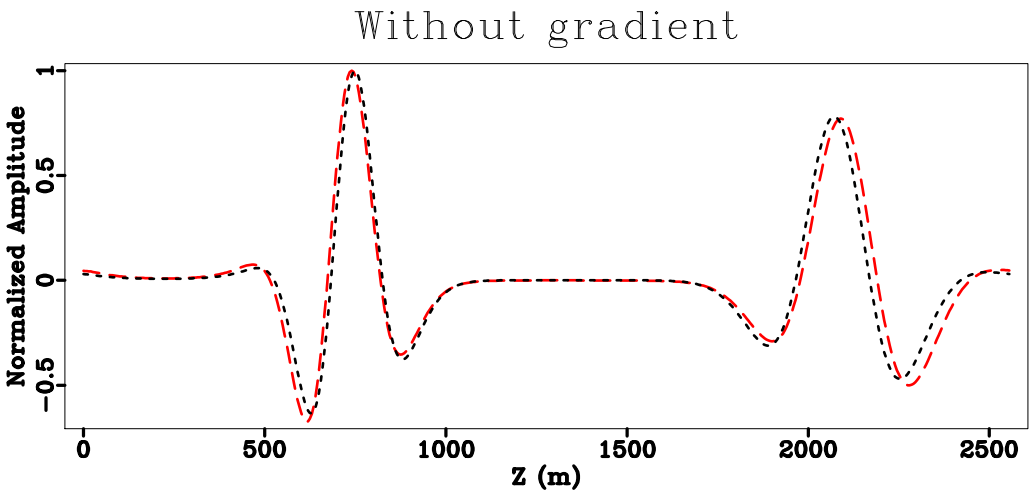

(b)

Figure 7: A slice through wavefields in Figure 6 at $X = 2000\ m$. The short-dashed line represents the reference wavefield; the solid line represents the result calculated with velocity gradient; the long-dashed line represents the result calculated without velocity gradient. grad/ compp,compp1

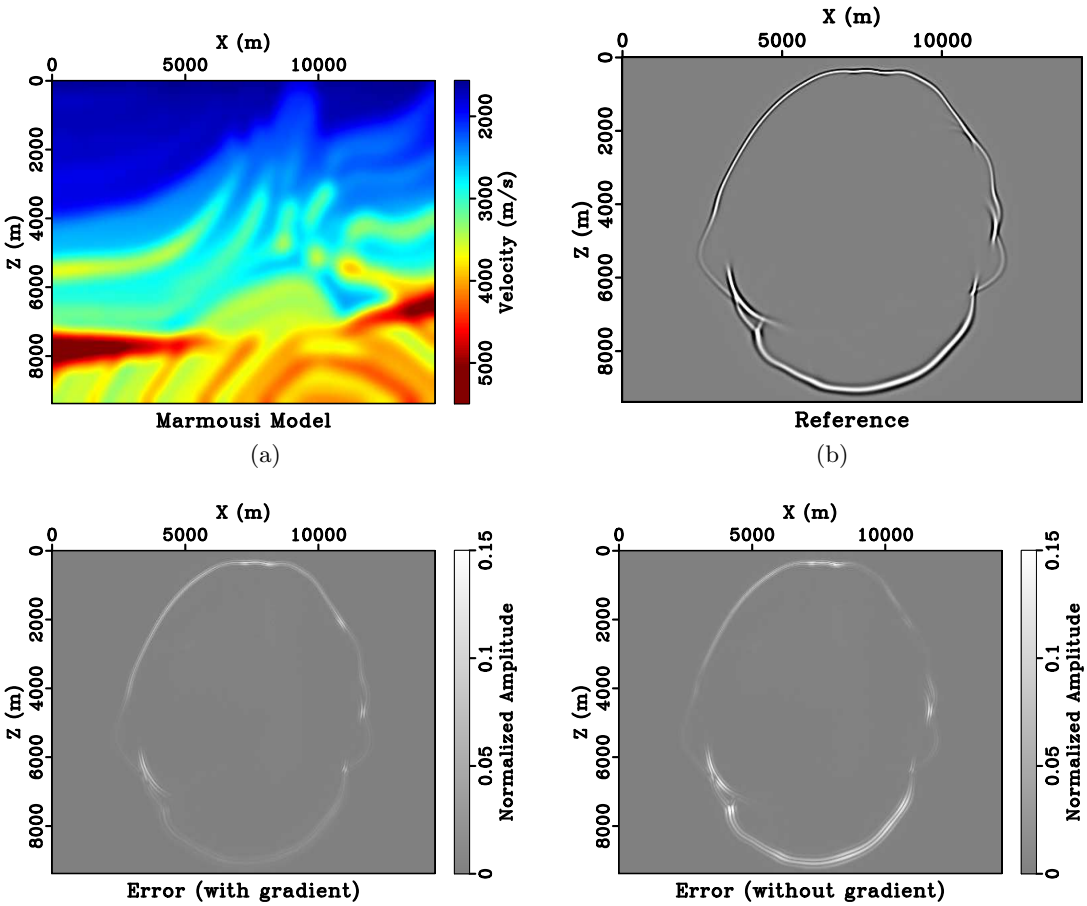

Figure 8: Wave propagation in a realistic velocity model. (a) Marmousi velocity model. (b) Reference wavefield propagated using $\Delta t = 1.5\ ms$. (c) Difference between the reference wavefield and the wavefield propagated with the velocity-gradient term using $\Delta t = 15\ ms$. (d) Difference between the reference wavefield and the wavefield propagated without the velocity-gradient term using $\Delta t = 15\ ms$. grad2/ mvel,wave1snap-b,mdiff,mdiff1

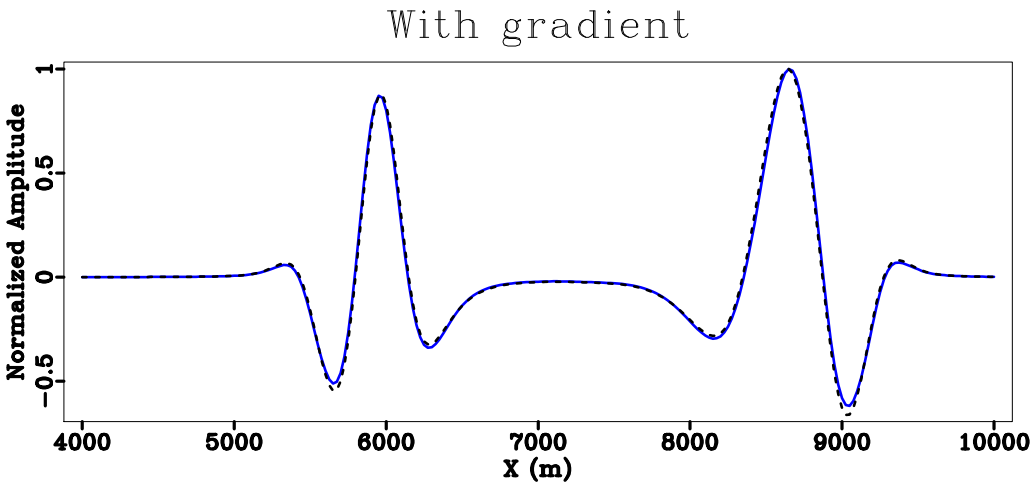

(a)

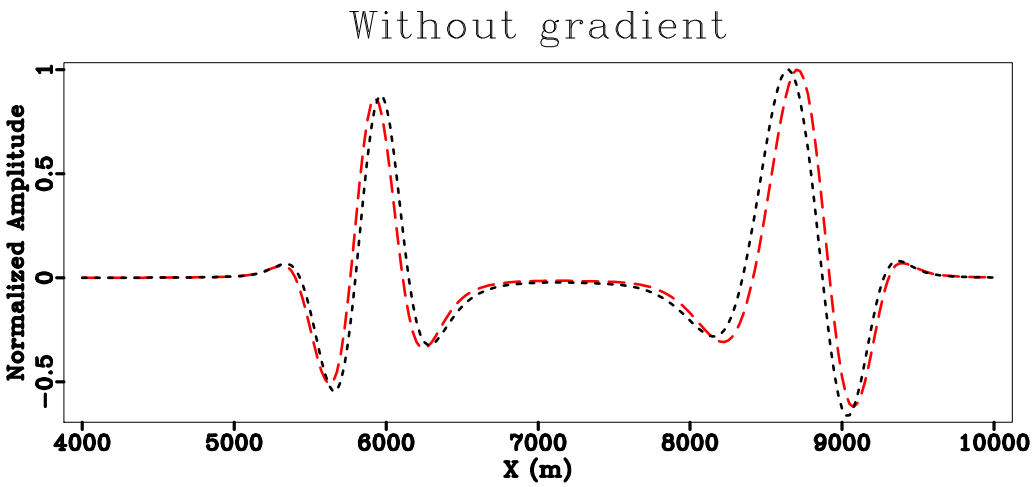

(b)

Figure 9: A slice through wavefields in Figure 8 at $X = 8800\ m$. The short-dashed line represents the reference wavefield; the solid line represents the result calculated with velocity gradient; the long-dashed line represents the result calculated without velocity gradient. grad2/ mcompp,mcompp1

In the remaining examples of this paper, the velocity gradient term was not included in the phase function for simplicity.

Absorbing boundary conditions

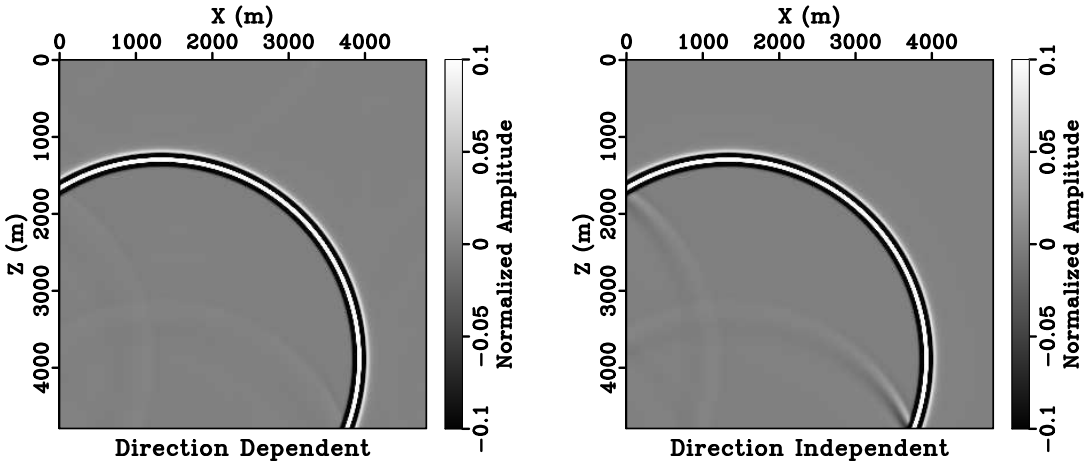

(a) (b)

Figure 10: Comparison between wavefield propagated with the direction-dependent absorbing boundary condition (a) and wavefield propagated with the direction-independent absorbing boundary condition (b). The amplitude has been normalized to 1, and the scale bar has been clipped to 0.1 to highlight artificial reflections from the boundary. abc/ cwavesnapgain,cwave2snapgain

In the next example, we incorporate the propagation-direction-dependent absorbing boundary condition in the wave extrapolation operator to attenuate waves reaching the boundary. The absorbing boundary defined by equation 26 does not attenuate any energy if the wave propagates parallel to the boundary, and reaches maximum damping when the wave propagates normal to the boundary. This property reduces artificial reflected energy at large incident angles. Figure 10 compares the propagation-direction-dependent absorbing boundary condition with a conventional direction-independent absorbing boundary condition (tapering) using a point-source wavefield. After normalization and clipping for display, the direction-dependent absorbing boundary condition proves to be more effective at wide-incident angles. In isotropic wave propagation, we observed that the direction-dependent absorbing boundary condition may increase the rank of the lowrank approximation because of induced anisotropic attenuation of wave propagation. One possible way to decrease the cost is to implement the absorbing boundary condition separately from the wave extrapolation process, using partial Fast Fourier Transforms (Ying and Fomel, 2009). In this way, the cost of absorbing boundaries can be marginal compared to the cost of wave extrapolation.

Wave propagation in TTI media

To show that the proposed method handles anisotropic media accurately, we propagate qP- and qSV-waves in a portion of the 2007 anisotropic benchmark model from BP. The model

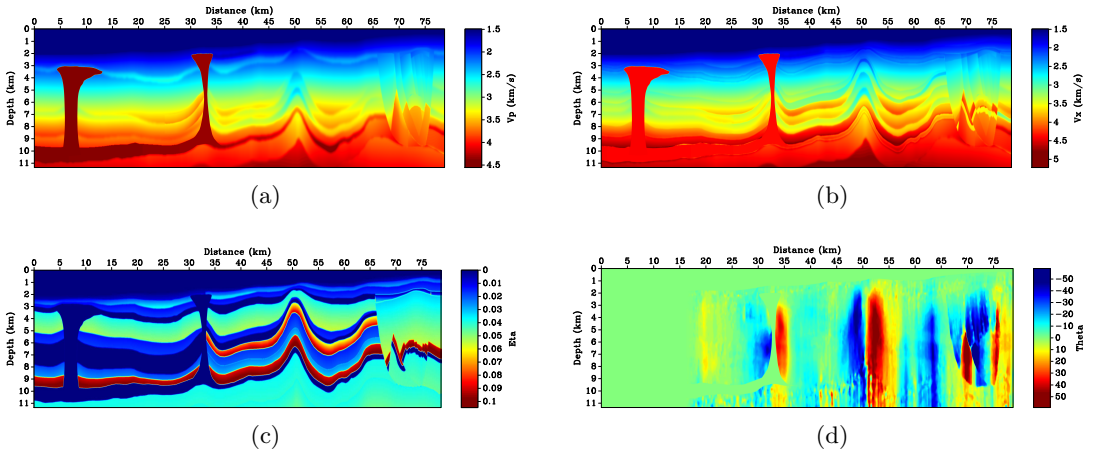

Figure 11: BP-2007 anisotropic benchmark model. (a) P-wave phase velocity along the axis of symmetry V_z. (b) P-wave phase in the symmetry plane V_x. (c) Anellipticity parameter η. (d) Tilt angle of the symmetry axis θ. bpttirtm/ vp,vx,eta,theta

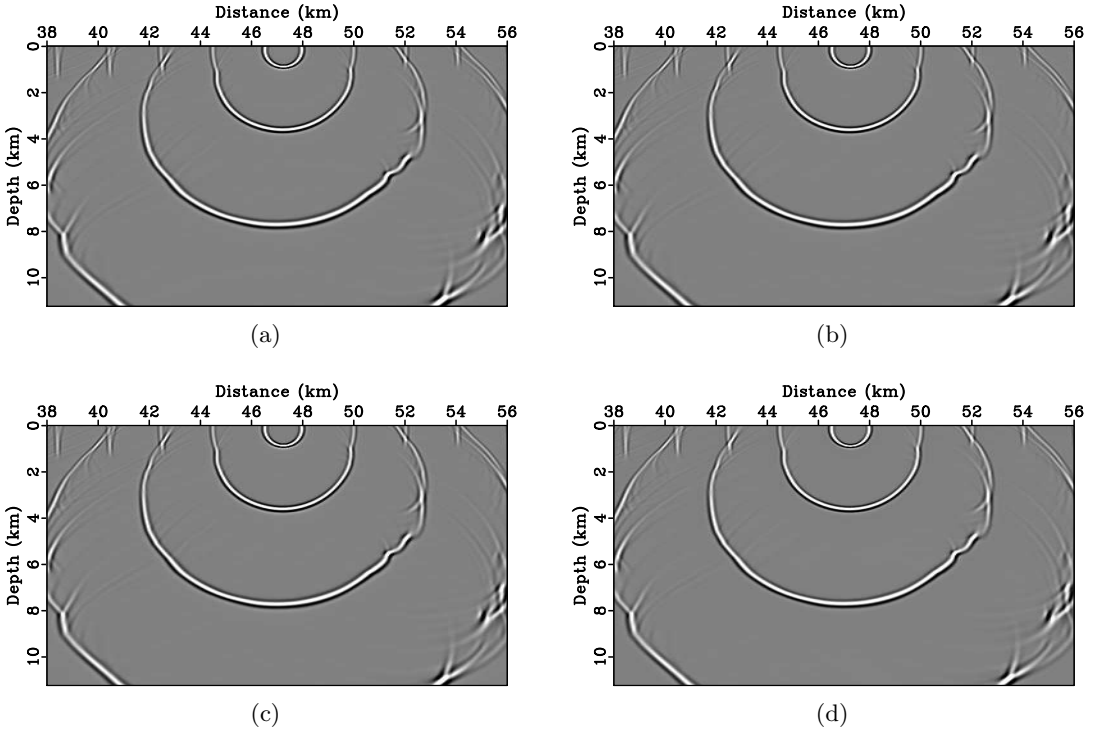

Figure 12: Wavefield snapshots taken at different times showing P-wave propagation through the 2007 BP TTI model. Propagation-direction-dependent absorbing boundary conditions allow little energy to be reflected, even at wide-incident angles. The four wavefield snapshots calculated using different time step sizes are almost identical: (a) $\Delta t = 4\ ms$; (b) $\Delta t = 10\ ms$; (c) $\Delta t = 20\ ms$; (d) $\Delta t = 30\ ms$. bptti2/ wavesnaps-4,wavesnaps-10,wavesnaps-20,wavesnaps-30

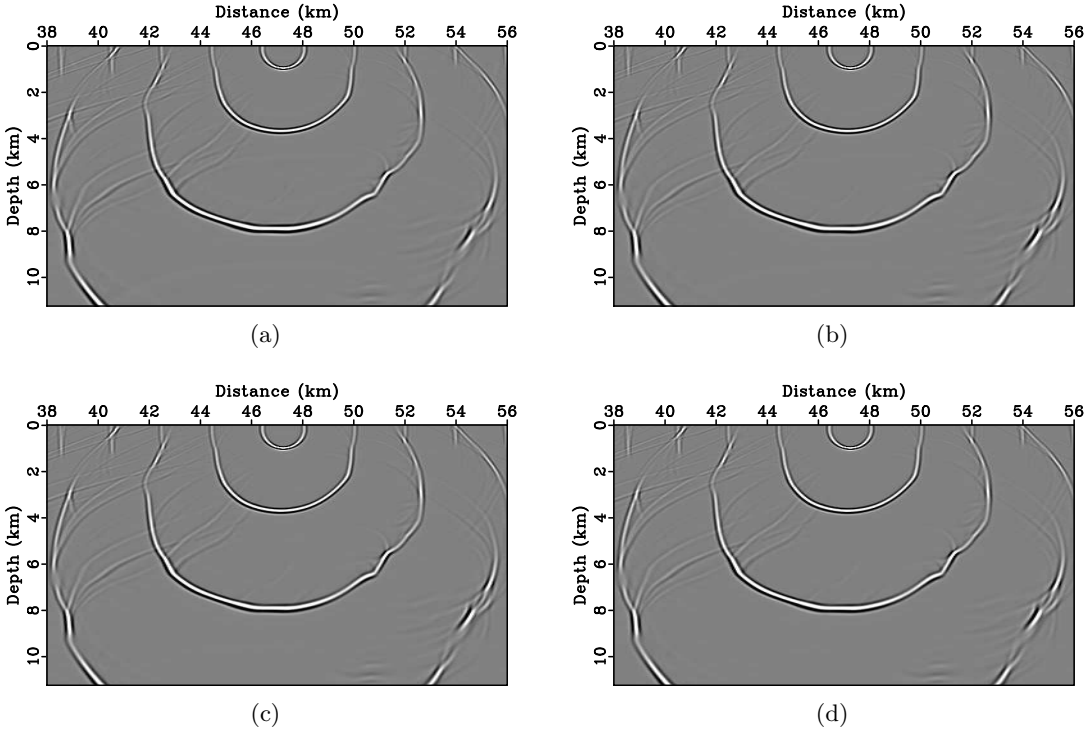

Figure 13: Wavefield snapshots taken at different times showing S-wave propagation through the 2007 BP TTI model. The four wavefield snapshots calculated using different time step sizes are almost identical: (a) $\Delta t = 2\ ms$; (b) $\Delta t = 4\ ms$; (c) $\Delta t = 10\ ms$; (d) $\Delta t = 20\ ms$. bptti/ swavesnaps-2,swavesnaps-4,swavesnaps-10,swavesnaps-20

has a horizontal spacing of 50 m and a vertical spacing of 25 m. As shown in Figure 11, the model exhibits a strong tilted transverse isotropy (TTI). We restrict the modeled area between 34 km and 60 km. Since the original model does not include S-wave velocity, we compute a vertical S-wave velocity profile simply as 0.3 times the original vertical P-wave velocity.

To calculate the qP- and qSV-wave phase velocities, we employ the exact formulas defined by Gassmann (1964):

$$\begin{aligned} V_P^2(\mathbf{n},\mathbf{x})|\mathbf{k}|^2 &= \frac{1}{2}\left[(c_{11}+c_{55})\,\hat{k}_x+(c_{33}+c_{55})\,\hat{k}_z\right]+ \\ &\quad \frac{1}{2}\sqrt{\left[(c_{11}-c_{55})\,\hat{k}_x-(c_{33}-c_{55})\,\hat{k}_z\right]^2+4\,(c_{13}+c_{55})^2\,\hat{k}_x\,\hat{k}_z}\;; \quad (31) \\ V_{SV}^2(\mathbf{n},\mathbf{x})|\mathbf{k}|^2 &= \frac{1}{2}\left[(c_{11}+c_{55})\,\hat{k}_x+(c_{33}+c_{55})\,\hat{k}_z\right]- \\ &\quad \frac{1}{2}\sqrt{\left[(c_{11}-c_{55})\,\hat{k}_x-(c_{33}-c_{55})\,\hat{k}_z\right]^2+4\,(c_{13}+c_{55})^2\,\hat{k}_x\,\hat{k}_z}\;, \quad (32) \end{aligned}$$

where c_{11}, c_{13}, c_{33} and c_{55} are the density-normalized components of the elastic tensor, $\mathbf{k}$ is the wavenumber vector, $\hat{k}_x$ and $\hat{k}_z$ are the wavenumbers evaluated in the rotated coordinate aligned with the symmetry axis:

$$\begin{aligned} \hat{k}_x &= k_x\cos\theta + k_z\sin\theta\;, \\ \hat{k}_z &= k_z\cos\theta - k_x\sin\theta\;, \end{aligned} \quad (33)$$

where θ is the tilt angle measured with respect to the horizontal direction. Alternatively, the qP-wave phase velocity can be calculated using accurate approximate formulas (Alkhalifah, 1998, 2000; Fomel, 2004; Sripanich and Fomel, 2015).

To mimic an unbounded medium, we apply the absorbing boundary condition in equation 26. First, a time step size of 4 ms for qP-wave and 2 ms for qSV-wave is used. A Ricker wavelet source with a peak frequency of 16 Hz is located at $X = 47.3$ km and $Z = 0.175$ km. Figures 12a and 13a illustrates wavefield snapshots taken at different times overlaid on top of each other. Because of the accumulative effect of the large time step, model complexity and extra anisotropy introduced by the absorbing boundary conditions, the lowrank approximation took $N = 19$ for qP-wave and $N = 15$ for qSV-wave for an accuracy threshold of $\epsilon = 10^{-4}$.

To test the effect of using large Δt for wave propagation, we choose a series of increasing Δt while enforcing the same accuracy requirement ($\epsilon = 10^{-4}$). The qP-wave wavefields (Figure 12) generated using $\Delta t = 4\ ms, 10\ ms, 20\ ms$ and $30\ ms$ are almost identical. Similarly, the qSV-wave wavefields (Figure 13) generated using $\Delta t = 2\ ms, 4\ ms, 10\ ms$ and $20\ ms$ have very little difference. This shows that the stability and accuracy of wave extrapolation is not compromised by using very large time steps, even beyond the Nyquist limit of 10 ms.

To investigate the effects of time step size (Δt) and accuracy level (ϵ) of lowrank approximation on the computational cost, which is directly controlled by the rank of the approximation, we conduct a series of experiments using different values of Δt and ϵ for qP-wave propagation. No absorbing boundary condition is applied in this test. Table 1 lists rank N required by different time step sizes to achieve different accuracy levels. We

can observe that the lowrank algorithm requires a higher rank to maintain the same level of accuracy when the time step size increases. On the other hand, with the same time step size, a higher rank may be needed to achieve a higher accuracy. In practice, we find that $\epsilon = 10^{-4}$ is small enough to guarantee accurate wave kinematics. Since making a larger step in time requires a smaller number of steps, the optimal time step size Δt can be selected to be the one that minimizes the total number of Fast Fourier Transforms (FFTs) required to accomplish the modeling or imaging task at hand. In practice, we found that this minimization problem usually has a straightforward solution: the larger Δt is, the less computation is required. Therefore, the optimal solution will be the largest Δt that satisfies other constraints, such as the imaging condition when performing RTM.

ϵ \ Δt(ms)	0.5	1	2	4	8	16	32	64
10^{-3}	4	7	7	10	14	19	33	53
10^{-4}	7	9	13	15	22	30	46	76
10^{-5}	11	14	18	23	30	43	59	84

Table 1: Rank N calculated from the lowrank approximation of the propagation matrix for qP-wave propagation in the BP 2007 TTI model using different time step sizes Δt and accuracy levels ϵ.

Wave propagation in 3D orthorhombic media

To demonstrate 3D wave propagation in tilted orthorhombic media, we use the classic model from Schoenberg and Helbig (1997), which characterizes a TI medium with vertical fractures. The density-normalized orthorhombic stiffness matrix is (Schoenberg and Helbig, 1997):

$$\begin{bmatrix} 9 & 3.6 & 2.25 & 0 & 0 & 0 \\ 3.6 & 9.84 & 2.4 & 0 & 0 & 0 \\ 2.25 & 2.4 & 5.9375 & 0 & 0 & 0 \\ 0 & 0 & 0 & 2 & 0 & 0 \\ 0 & 0 & 0 & 0 & 1.6 & 0 \\ 0 & 0 & 0 & 0 & 0 & 2.182 \end{bmatrix} \tag{34}$$

To introduce spatial heterogeneity, we apply a moderate perturbation to the stiffness coefficients that is a function of $\mathbf{x}$, as demonstrated by Figure 14 for the case of C_{11}. The model is further rotated 45 ° counterclockwise about the Z axis (azimuth angle) and 45 ° counterclockwise about the X axis (dip angle).

We employ the exact phase velocity in orthorhombic media (Tsvankin, 1997):

$$V^2(\mathbf{x},\mathbf{k})|\mathbf{k}|^2 = 2\sqrt{\frac{a^2/3-b}{3}}\cos\left(\frac{\upsilon}{3}+n\frac{2\pi}{3}\right)-\frac{a}{3}\,, \tag{35}$$

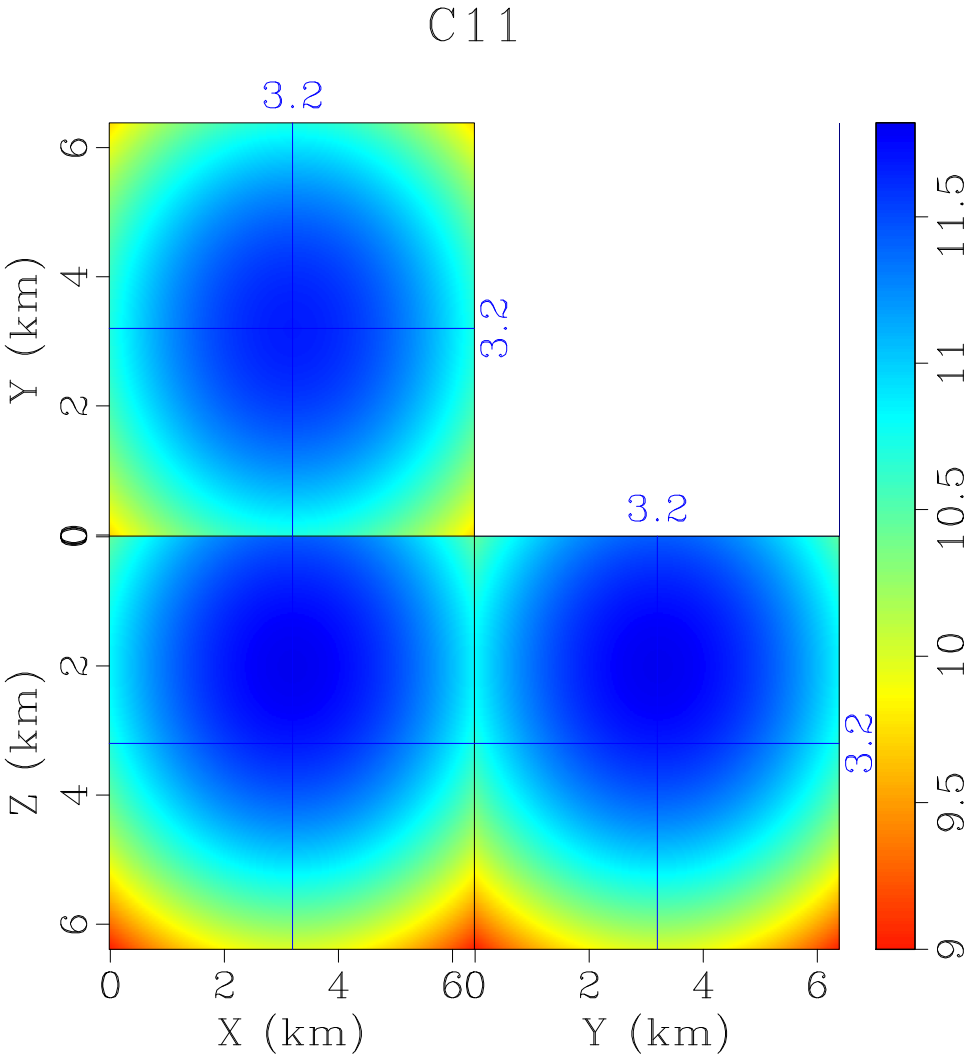

Figure 14: The perturbed C_{11} coefficient in the orthorhombic test. All other stiffness coefficients are perturbed in a similar manner. tiltorth/ c11

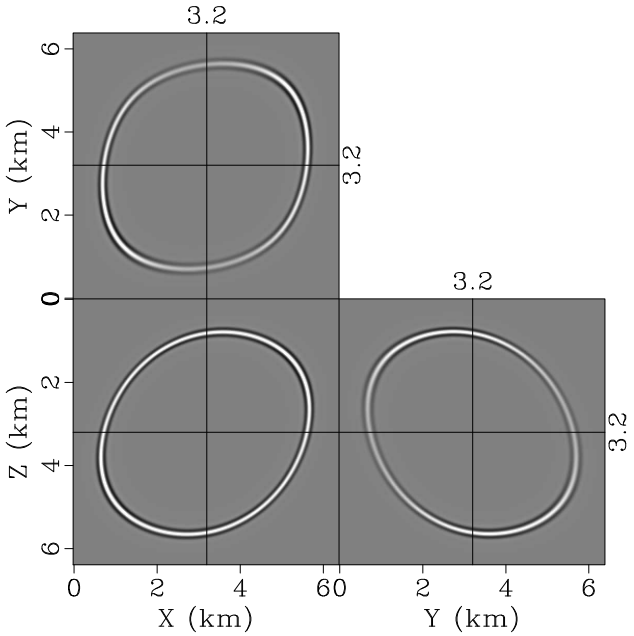

(a)

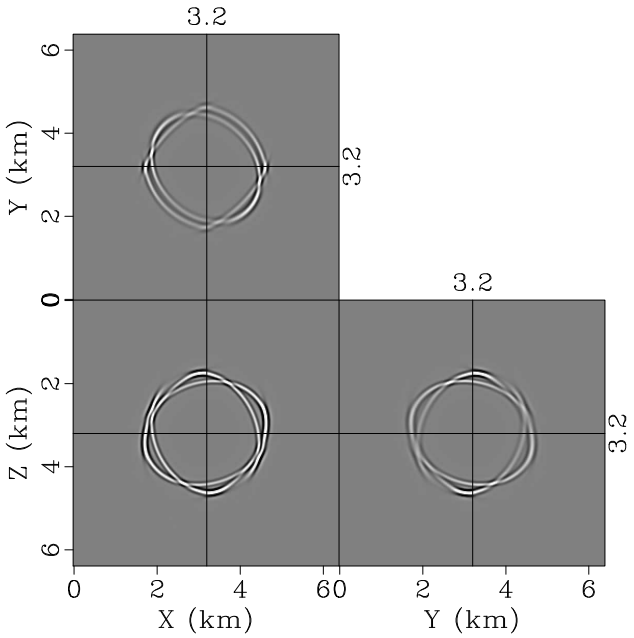

(b)

Figure 15: Wavefield snapshot of wave propagation in orthorhombic media taken at $t = 1s$: (a) qP-wave, (b) Coupled qS-waves. tiltorth/ wavec-0,wavecs

where $n = 0$ corresponds to the P wave and $n = 1, 2$ corresponds to the shear waves, and

$$\upsilon = \arccos\left(-\frac{2(a/3)^3 - ab/3 + c}{2\sqrt{((a^2/3 - b)/3)^3}}\right) \ (0 \le \upsilon \le \pi) \ , \tag{36}$$

$$a = -(G_{11} + G_{22} + G_{33}) \ , \tag{37}$$

$$b = G_{11}G_{22} + G_{11}G_{33} + G_{22}G_{33} - G_{12}^2 - G_{13}^2 - G_{23}^2 \ , \tag{38}$$

$$c = G_{11}G_{23}^2 + G_{22}G_{13}^2 + G_{33}G_{12}^2 - G_{11}G_{22}G_{33} - 2G_{12}G_{13}G_{23} \ , \tag{39}$$

$$G_{11} = c_{11}\hat{k}_x^2 + c_{66}\hat{k}_y^2 + c_{55}\hat{k}_z^2 \ , \tag{40}$$

$$G_{22} = c_{66}\hat{k}_x^2 + c_{22}\hat{k}_y^2 + c_{44}\hat{k}_z^2 \ , \tag{41}$$

$$G_{33} = c_{55}\hat{k}_x^2 + c_{44}\hat{k}_y^2 + c_{33}\hat{k}_z^2 \ , \tag{42}$$

$$G_{12} = (c_{12} + c_{66})\hat{k}_x\hat{k}_y \ , \tag{43}$$

$$G_{13} = (c_{13} + c_{55})\hat{k}_x\hat{k}_z \ , \tag{44}$$

$$G_{23} = (c_{23} + c_{44})\hat{k}_y\hat{k}_z \ . \tag{45}$$

To incorporate tilting into the orthorhombic anisotropy, we replace the original wavenumber components k_x, k_y and k_z with $\hat{k}_x$, $\hat{k}_y$, and $\hat{k}_z$, which are wavenumbers evaluated in the rotated coordinate system aligned with the symmetry axis:

$$\begin{aligned} \hat{k}_x &= k_x \cos\phi + k_y \sin\phi \ , \\ \hat{k}_y &= -k_x \sin\phi \cos\theta + k_y \cos\phi \cos\theta + k_z \sin\theta \ , \\ \hat{k}_z &= k_x \sin\phi \sin\theta - k_y \cos\phi \sin\theta + k_z \cos\theta \ , \end{aligned} \tag{46}$$

where ϕ is the azimuth angle representing horizontal rotation (the angle between the original X axis and the rotated one) and θ is the dip angle measured from vertical. Figure 15 demonstrates the wavefield snapshots taken at $t = 1$ s for three wave modes: quasi-P-wave and the coupled quasi-S-waves. Note that the quasi-S-waves are propagated separately using solutions from equation 35 and then summed together, since the two modes do not decouple easily in an orthorhombic medium.

RTM of BP 2007 TTI Data Set

Finally, we test lowrank one-step RTM using BP 2007 anisotropic benchmark dataset (Figure 11). The grid spacing is 18.75 m in the horizontal direction and 12.5 m in the vertical direction. The time step size is selected to be 4 ms. We employ the acoustic approximation (Alkhalifah, 1998, 2000; Fomel, 2004) to calculate the qP-wave phase velocity. The sedimentary layers, salt boundaries, anticline and fault surfaces are clearly imaged by the lowrank one-step RTM method (Figure 16).

DISCUSSION

The modeling experiments using an isotropic two-layer model and a portion of BP 2007 TTI benchmark model show that the proposed operator is in practice remarkably stable and accurate. When the velocity contrast is not very sharp, the lowrank one-step method is capable of propagating waves free of dispersion artifacts using time steps even larger than

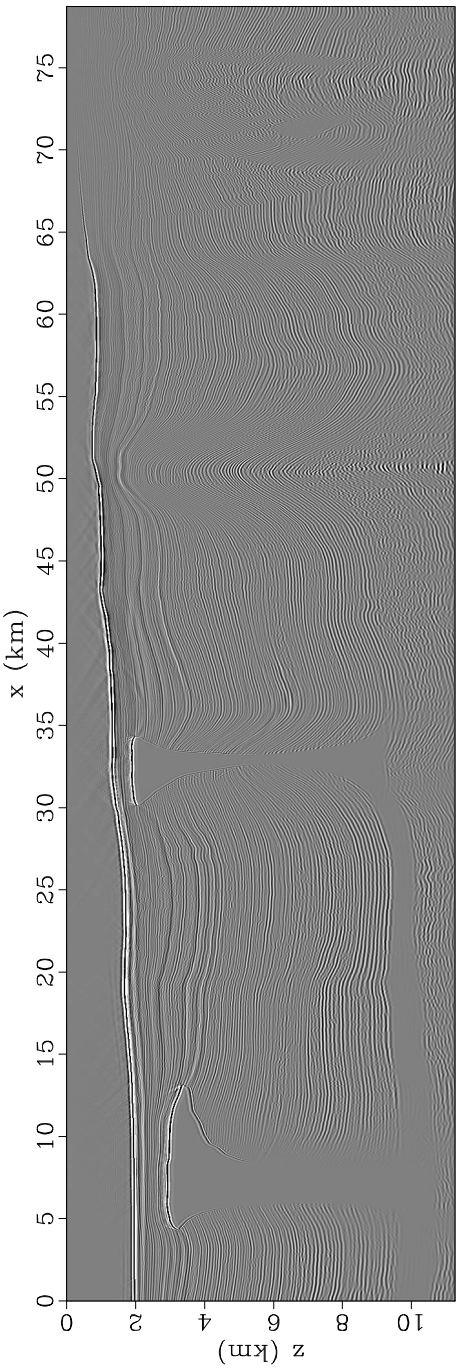

Figure 16: RTM image obtained using BP 2007 anisotropic data set. Acoustic approximation in TI medium is used to perform wave extrapolation. bpttirtm/ bptti-img

the Nyquist sampling limit of the source wavelet. The maximum efficiency can be achieved using the largest step size possible, which in RTM applications usually corresponds to the time sampling of the imaging condition. In contrast, conventional approaches, such as high-order finite-difference and pseudo-spectral methods, are confined to small step sizes due to severe stability and accuracy constraints. This is especially true when S-wave extrapolation is required by RTM, because the slow S-wave velocity at shallow depths imposes a strict constraint on the time step size of conventional methods. Lowrank one-step wave extrapolation has been recently applied to converted wave imaging by Casasanta et al. (2015) and achieved accurate results.

Our numerical experiments confirm advantages of the lowrank one-step wave extrapolation over the two-step scheme. By extrapolating an analytical wavefield with the imaginary part related to the first derivative of the real-valued wavefield, the one-step scheme is capable of using a much larger time step size (Du et al., 2014). The complex phase function used by the lowrank one-step method offers additional freedom in the design of the wave extrapolation operator. In media with smoothly varying velocities, a large time step may impair accuracy using the conventional formulation. By using a more accurate expression, for example by admitting more terms from the Taylor expansion of the phase function, the lowrank one-step wave extrapolation can achieve higher accuracy. The complex-valued extrapolation operator also allows for an effective mixed-domain absorbing boundary condition, which dampens wave energy according to the phase direction and thus avoids artificial reflections at large incident angles. The application of a complex phase function is not limited to the proposed cases. Another possible extension is seismic modeling and imaging in visco-acoustic media (Zhu and Harris, 2014), where the one-step extrapolator solves a complex-valued, decoupled dispersion relation that incorporates attenuation effects (Sun et al., 2014, 2015).

CONCLUSIONS

We have developed lowrank wave extrapolation using a one-step scheme. The one-step lowrank method appears to be more stable than the two-step method, and exhibits superior stability in numerical experiments. The capability of propagating waves using large time steps can help saving costs when performing modeling, imaging or full waveform inversion tasks. We propose two modifications to the complex phase function, which can be accurately handled by the lowrank one-step approach. First, we show that, when the velocity-gradient term is included in the approximation of the phase function, a higher accuracy can be achieved. Next, we use a one-step scheme to incorporate a propagation-direction-dependent absorbing boundary condition in the wave propagation operator, which reduces artificial reflections at wide-incident angles. Numerical examples using simple models demonstrate the improved accuracy and efficiency of the proposed method. In particular, we apply the lowrank one-step operator to wave extrapolation in 2D TTI media and 3D orthorhombic media, and obtain wavefields free of dispersion artifacts or residual shear-wave artifacts. When lowrank one-step RTM is applied on the BP 2007 TTI benchmark data set, it produces high-quality seismic images.

ACKNOWLEDGMENTS

We thank Zedong Wu and one anonymous reviewer for their constructive comments. We would like to also thank Jiubing Cheng, Gang Fang, Paul Fowler, Jingwei Hu, Siwei Li, Xiaolei Song and Zhiguang Xue for inspiring discussions. We thank the sponsors of the Texas Consortium for Computational Seismology (TCCS) for financial support. The first author was additionally supported by the Statoil Fellows Program at the University of Texas at Austin. The BP 2007 benchmark data set was created by Hemang Shah and released by BP Exploration Operation Co., Ltd. We thank Texas Advanced Computing Center (TACC) for providing computational resources used in this study.

APPENDIX A: PROOF OF THE STABILITY OF ONE-STEP WAVE EXTRAPOLATION OPERATOR

In this appendix, we prove the unconditional stability of one-step wave extrapolation linear operator $u = \mathbf{L}f$ in one-dimensional isotropic media defined by:

$$u(x) = \sum_{\xi \in z} e^{2\pi i(x\xi + V(x)|\xi|t)} \hat{f}(\xi) \quad \text{for} \quad f(x) \in l^2[0,1] \; , \tag{47}$$

where $2\pi\xi = \mathbf{k}$, $f(x)$ is assumed to have periodic boundary condition, and $\hat{f}(\xi)$ is the Fourier transform of $f(x)$ as defined by equation 3. We treat ξ as discrete and x as continuous for the ease of derivation. Our argument can be viewed as a discrete version of the standard stationary phase method in the study of pseudodifferential operators Grigis and Sjöstrand (1994); Stein (1993). To show that the operator $\mathbf{L}$ is stable, a sufficient condition is that $\|\mathbf{L}\|_{2\to 2} \leq 1 + Ct$, where C is a bounded constant. From equation 47, we observe that operator $\mathbf{L}$ is the composition of two operators $\mathbf{L} = \mathbf{AF}$, where F is the inverse Fourier transform and $\mathbf{A}$ is the operator defined by:

$$(\mathbf{A}\omega)(z) = \sum_{\xi \in z} e^{2\pi i(x\xi + V(x)|\xi|t)} \omega(\xi) \quad \text{for} \quad \omega \in l^2(z) \; . \tag{48}$$

Let us consider $\mathbf{A}^\intercal\mathbf{A} : l^2 \to l^2$ where $\mathbf{A}$ corresponds to a matrix with (x, ξ) entry given by $\mathbf{A}(x,\xi) = e^{2\pi i(x\xi + V(x)|\xi|t)}$, and $\mathbf{A}^\intercal$ corresponds to a matrix with (η, x) entry given by $\mathbf{A}^\intercal(\eta, x) = e^{-2\pi i(x\eta + V(x)|\eta|t)}$. $\mathbf{A}^\intercal\mathbf{A}$ represents a matrix with (η, ξ) entry given by:

$$\mathbf{A}^\intercal\mathbf{A}(\eta,\xi) = \int e^{2\pi i[x(\xi-\eta) + V(x)(|\xi|-|\eta|)t]} dx \; . \tag{49}$$

In order to bound the $l^2 \to l^2$ norm of $\mathbf{A}^\intercal\mathbf{A}$ we estimate the (η, ξ) entry of $\mathbf{A}^\intercal\mathbf{A}$. For $\xi = \eta$, we have $\mathbf{A}^\intercal\mathbf{A}(\eta,\xi) = 1$. For $\xi \neq \eta$:

$$x(\xi - \eta) + V(x)(|\xi| - |\eta|)t = x(\xi - \eta) + V(x)\alpha(\xi - \eta)t \; , \tag{50}$$

with $\alpha = (|\xi| - |\eta|)/(\xi - \eta)$. Clearly, $|\alpha| \leq 1$. Then $\mathbf{A}^\intercal\mathbf{A}$ can be expressed as

$$\mathbf{A}^\intercal\mathbf{A}(\eta,\xi) = \int e^{2\pi i(\xi-\eta)[x + V(x)\alpha t]} dx \tag{51}$$

For sufficiently small t, $x + V(x)\alpha t$ satisfies

$$\frac{1}{2} \leq \nabla_x \left[x + V(x)\alpha t\right] \leq \frac{3}{2} \,. \tag{52}$$

Equation 51 can be expressed as:

$$\begin{aligned} \mathbf{A}^\intercal\mathbf{A}(\eta,\xi) &= \int e^{2\pi i(\xi-\eta)[x+V(x)\alpha t]} \frac{1+V'(x)\alpha t}{1+V'(x)\alpha t} dx \\ &= \int \frac{1}{1+V'(x)\alpha t} e^{2\pi i(\xi-\eta)[x+V(x)\alpha t]} d\left[x+V(x)\alpha t\right] \,. \end{aligned} \tag{53}$$

Let us define $y = x + V(x)\alpha t$. From equation 52, it is clear that the map $x \leftrightarrow y$ is one to one. Substituting y into equation 53 gives

$$\mathbf{A}^\intercal\mathbf{A}(\eta,\xi) = \int \frac{1}{1+V'(x(y))\alpha t} e^{2\pi i(\xi-\eta)y} dy \,, \tag{54}$$

which is the inverse Fourier transform of $\frac{1}{1+V'(x(y))\alpha t}$. When t is small,

$$\begin{aligned} \mathbf{A}^\intercal\mathbf{A}(\eta,\xi) &= \int \left[1 - V'(x(y)\alpha t + \mathcal{O}(t^2))\right] e^{2\pi i(\xi-\eta)y} dy \\ &= -\alpha t \int V'(x(y)) e^{2\pi i(\xi-\eta)y} dy + \mathcal{O}(t^2) \,. \end{aligned} \tag{55}$$

To evaluate the norm of the integration term in the last equation, we perform integration by part for k-times and apply periodic boundary condition:

$$\left| \int V'(x(y)) e^{2\pi i(\xi-\eta)y} dy \right| \leq \frac{1}{(2\pi|\xi-\eta|)^k} \int e^{2\pi i(\xi-\eta)y} \left| \partial_y^k V'(x(y)) \right| dy \,. \tag{56}$$

Assuming sufficient smoothness on $V(x)$, we have for $\xi \neq \eta$

$$|(\mathbf{A}^\intercal\mathbf{A} - \mathbf{I})(\eta,\xi)| \leq \frac{Ct}{|\xi-\eta|^k}, \tag{57}$$

for a constant C. To estimate the $l^2 \to l^2$ norm of $\mathbf{A}^\intercal\mathbf{A}$, we make use of the following lemma which can be derived from direct calculation.

Lemma 1. *Suppose* $\mathbf{G} : l^2 \to l^2$ *with* $\sum_\xi |\mathbf{G}(\xi,\eta)| \leq C$ *and* $\sum_\eta |\mathbf{G}(\xi,\eta)| \leq C$*, then* $\mathbf{G}$ *is a bounded* $l^2 \to l^2$ *operator.*

We now apply the above lemma to $\mathbf{A}^\intercal\mathbf{A} - \mathbf{I}$. When $k \geq d$ where d is the spatial dimension, we have $\sum_{\xi\neq\eta} \frac{C}{|\xi-\eta|^k}$ bounded. Therefore, for sufficiently smooth V, we have $\|\mathbf{A}^\intercal\mathbf{A} - \mathbf{I}\|_{2\to2} \leq Ct$, for suffciently small t. Hence $\|\mathbf{A}^\intercal\mathbf{A}\|_{2\to2} \leq 1 + Ct$ and $\|\mathbf{A}\|_{2\to2} \leq 1 + Ct$. Since $\mathbf{L} = \mathbf{AF}$ and $\mathbf{F}$ as the Fourier transform is an isometry, we have $\|\mathbf{L}\|_{2\to2} \leq 1 + Ct$.

When performing wave extrapolation, fix a final time T and propagate T/dt steps, the operator is stable since

$$\|\mathbf{L}^{T/t}\|_{2\to2} \leq (1+Ct)^{T/t} \leq e^{CT}. \tag{58}$$

REFERENCES

Alkhalifah, T., 1998, Acoustic approximations for processing in transversely isotropic media: Geophysics, **63**, 623–631.

———, 2000, An acoustic wave equation for anisotropic media: Geophysics, **65**, 1239–1250.

Baysal, E., D. D. Kosloff, and J. W. C. Sherwood, 1983, Reverse time migration: Geophysics, **48**, 1514–1524.

Casasanta, L., Z. Xue, and S. H. Gray, 2015, Converted wave RTM using lowrank wavefield extrapolation: 77th Annual EAGE Meeting, EAGE, Expanded Abstracts, N116.

Cerjan, C., D. Kosloff, R. Kosloff, and M. Reshef, 1985, A nonreflecting boundary condition for discrete acoustic and elastic wave equations: Geophysics, **50**, 705–708.

Chu, C., and P. L. Stoffa, 2011, Compensating for time stepping errors locally in the pseudo- analytical method using normalized pseudo-Laplacian: 81st Annual International Meeting, SEG, Expanded Abstracts, 3059–3063.

Claerbout, J. F., 1985, Imaging the Earth's interior: Blackwell Scientific Publications.

Du, X., R. P. Fletcher, and P. J. Fowler, 2010, Pure P-wave propagators versus pseudo-acoustic propagators for RTM in VTI meida: 72nd Annual EAGE Meeting, EAGE, Expanded Abstracts, C013.

Du, X., P. J. Fowler, and R. P. Fletcher, 2014, Recursive integral time-extrapolation methods for waves: A comparative review: Geophysics, **79**, no. 1, T9–T26.

Etgen, J., and S. Brandsberg-Dahl, 2009, The pseudo-analytical method: application of pseudo-Laplacians to acoustic and acoustic anisotropic wave propagation: 79th Annual International Meeting, SEG, Expanded Abstracts, 2552–2556.

Etgen, J., S. Gray, and Y. Zhang, 2009, An overview of depth imaging in exploration geophysics: Geophysics, **74**, no. 6, WCA5–WCA17.

Fang, G., S. Fomel, Q. Du, and J. Hu, 2014, Lowrank seismic wave extrapolation on a staggered grid: Geophysics, **79**, no. 3, T157–T168.

Farmer, P. A., I. F. Jones, H. Zhou, R. I. Bloor, and M. C. Goodwin, 2006, Application of reverse time migration to complex imaging problems: First Break, **24**, 65–73.

Fletcher, R. P., X. Du, and P. J. Fowler, 2009, Reverse time migration in tilted transversely isotropic (TTI) media: Geophysics, **74**, no. 6, WCA179–WCA187.

Fomel, S., 2004, On anelliptic approximations for qP velocities in VTI media: Geophysical Prospecting, **52**, 247–259.

Fomel, S., L. Ying, and X. Song, 2010, Seismic wave extrapolation using a lowrank symbol approximation: 80th Annual International Meeting, SEG, Expanded Abstracts, 3092–3096.

———, 2013, Seismic wave extrapolation using lowrank symbol approximation: Geophysical Prospecting, **61**, no. 3, 526–536.

Fornberg, B., 1998, A practical guide to pseudospectral methods: Cambridge university press, **1**.

Fowler, P. J., X. Du, and R. P. Fletcher, 2010a, Coupled equations for reverse time migration in transversely isotropic media: Geophysics, **75**, no. 1, S11–S22.

———, 2010b, Recursive integral time extrapolation methods for scalar waves: 80th Annual International Meeting, SEG, Expanded Abstracts, 3210–3215.

Gassmann, F., 1964, Introduction to seismic travel time methods in anisotropic media: Pure and Applied Geophysics, **58**, 63–112.

Grigis, A., and J. Sjöstrand, 1994, Microlocal analysis for differential operators: Cambridge University Press, Cambridge, volume **196** *of* London Mathematical Society Lecture Note

Series. (An introduction).

Kosloff, D., and E. Baysal, 1982, Forward modeling by a Fourier method: Geophysics, **47**, 1402–1412.

Leveille, J. P., I. F. Jones, Z. Z. Zhou, B. Wang, and F. Liu, 2011, Subsalt imaging for exploration, production, and development: A review: Geophysics, **76**, no. 5, WB3–WB20.

Liu, F., S. A. Morton, S. Jiang, L. Ni, and J. P. Leveille, 2009, Decoupled wave equations for P and SV waves in an acoustic VTI media: 79th Annual International Meeting, SEG, Expanded Abstracts, 2844–2848.

McMechan, G. A., 1983, Migration by extrapolation of time-dependent boundary values: Geophysical Prospecting, **31**, 413–420.

Pestana, R. C., and P. L. Stoffa, 2010, Time evolution of the wave equation using rapid expansion method: Geophysics, **75**, no. 4, T121–T131.

Reshef, M., D. Kosloff, M. Edwards, and C. Hsiung, 1988, Three-dimensional acoustic modeling by the Fourier method: Geophysics, **53**, 1175–1183.

Rickett, J., and P. Sava, 2002, Offset and angle-domain common image-point gathers for shot-profile migration: Geophysics, **67**, no. 3, 883–889.

Sava, P., and S. Fomel, 2003, Angle-domain common image gathers by wavefield continuation methods: Geophysics, **68**, 1065–1074.

———, 2006, Time-shift imaging condition in seismic migration: Geophysics, **71**, no. 6, S209–S217.

Sava, P., and I. Vasconcelos, 2011, Extended imaging conditions for wave-equation migration: Geophysical Prospecting, **59**, 35–55.

Schoenberg, M., and K. Helbig, 1997, Orthorhombic media: Modeling elastic wave behavior in a vertically fractured earth: Geophysics, **62**, no. 6, 1954–1974.

Song, X., S. Fomel, and L. Ying, 2013, Lowrank finite-differences and lowrank Fourier finite-differences for seismic wave extrapolation: Geophysical Journal International, **193**, no. 2, 960–969.

Soubaras, R., and Y. Zhang, 2008, Two-step explicit marching method for reverse time migration: 78th Annual International Meeting, SEG, Expanded Abstracts, 2272–2276.

Sripanich, Y., and S. Fomel, 2015, On anelliptic approximations for qP velocities in transversely isotropic and orthorhombic media: Geophysics, **80**, no. 5, C89–C105.

Stein, E. M., 1993, Harmonic analysis: real-variable methods, orthogonality, and oscillatory integrals: Princeton University Press, Princeton, NJ, volume **43** *of* Princeton Mathematical Series. (With the assistance of Timothy S. Murphy, Monographs in Harmonic Analysis, III).

Sun, J., T. Zhu, and S. Fomel, 2014, Viscoacoustic modeling and imaging using low-rank approximation: 84th Annual International Meeting, SEG, Expanded Abstracts, 3997–4002.

———, 2015, Viscoacoustic modeling and imaging using low-rank approximation: Geophysics, **80**, no. 5, A103–A108.

Taner, M. T., F. Koehler, and R. E. Sheriff, 1979, Complex seismic trace analysis: Geophysics, **44**, no. 6, 1041–1063.

Tsvankin, I., 1997, Anisotropic parameters and P-wave velocity for orthorhombic media: Geophysics, **62**, no. 4, 1292–1309.

Virieux, J., H. Calandra, and R. Plessix, 2011, A review of the spectral, pseudo-spectral, finite-difference and finite-element modelling techniques for geophysical imaging: Geophysical Prospecting, **59**, 794–813.

Wards, B. D., G. F. Margrave, and M. P. Lamoureux, 2008, Phase-shift time-stepping for

reverse-time migration: 78th Annual International Meeting, SEG, Expanded Abstracts, 2262–2266.

Whitmore, N. D., 1983, Iterative depth migration by backward time propagation: 53rd Annual International Meeting, SEG, Expanded Abstracts, 382–385.

Wu, Z., and T. Alkhalifah, 2014, The optimized expansion based low-rank method for wavefield extrapolation: Geophysics, **79**, no. 2, T51–T60.

Ying, L., and S. Fomel, 2009, Fast computation of partial Fourier Transforms: Multiscale Model. Simul., **8**, no. 1, 110–124.

Zhang, Y., and G. Zhang, 2009, One-step extrapolation method for reverse time migration: Geophysics, **74**, no. 4, A29–A33.

Zhu, T., and J. M. Harris, 2014, Modeling acoustic wave propagation in heterogeneous attenuating media using decoupled fractional Laplacians: Geophysics, **79**, no. 3, T105–T116.